catalysts

MDPI

Article

Indoor Air Photocatalytic Decontamination by UV–Vis Activated CuS/SnO_2/WO_3 Heterostructure

Alexandru Enesca * and Viorel Sisman

Product Design, Mechatronics and Environmental Department, Transilvania University of Brasov, Eroilor 29 Street, 35000 Brasov, Romania; v.sisman@unitbv.ro

* Correspondence: aenesca@unitbv.ro

Abstract: A titania-free heterostructure based on CuS/SnO_2/WO_3 was obtained by a three-step sol–gel method followed by spray deposition on the glass substrate. The samples exhibit crystalline structures and homogenous composition. The WO_3 single-component sample morphology consists of fibers that serve as the substrate for SnO_2 development. The CuS/SnO_2/WO_3 heterostructure is characterized by a dense granular morphology. Photocatalytic activity was evaluated under UV–Vis radiation and indicates that the WO_3 single-component sample is able to remove 41.1% of acetaldehyde (64.9 ppm) and 52.5% of formaldehyde (81.4 ppm). However, the CuS/SnO_2/WO_3 exhibits a superior photocatalytic activity due to a larger light spectrum absorption and lower charge carrier recombination rate, allowing the removal of 69.2% of acetaldehyde and 78.5% of formaldehyde. The reusability tests indicate that the samples have a stable photocatalytic activity after three cycle (12 h/cycle) assessments. During light irradiation, the heterostructure acted as a Z-scheme mechanism using the redox ability of the CuS conduction band electrons and the SnO_2/WO_3 valence band holes to generate the oxidative species required for VOC removal.

Keywords: air decontamination; photocatalysis; semiconductors; acetaldehyde; formaldehyde

Citation: Enesca, A.; Sisman, V. Indoor Air Photocatalytic Decontamination by UV–Vis Activated CuS/SnO_2/WO_3 Heterostructure. *Catalysts* **2022**, *12*, 728. https://doi.org/10.3390/catal12070728

Academic Editors: Detlef W. Bahnemann, Wonyong Choi, Ioannis Konstantinou, Ewa Kowalska, Magdalena Janus, Vincenzo Vaiano and Zhi Jiang

Received: 7 June 2022
Accepted: 28 June 2022
Published: 30 June 2022

1. Introduction

Air contaminants such as nitric oxide (NO) and nitrogen dioxide (NO_2), originating mainly from industrial and transportation activities (incomplete fossil fuel combustion or vehicle exhaust emissions), cause significant problems related to ozone layer reduction, acid rain production, chemical smog appearance, and particle pollution [1–3]. However, indoor air is equally essential for human health, considering that more than 80% of our time is spent in closed spaces (homes, offices, halls, malls, libraries, etc.). Volatile organic compounds (VOCs) are the main indoor air pollutants that directly impact human health [4,5]. VOCs are composed of aromatics, alcohols, halocarbons, and aldehydes, which are essential components of building materials, furniture, and electronic equipment. Several studies indicate that long-term exposure to VOCs can induce acute and chronic health problems. The risk of inhaling VOCs in indoor spaces is higher compared to outdoors, causing symptoms such as allergies, dizziness, nausea, wheezing, coughing, and headaches [6–8].

The removal of these pollutants from indoor spaces is urgent considering that access to VOC sources, such as electronic equipment and furniture, is more affordable in many countries due to economic expansion. Traditional VOC removal technologies, such as adsorption, biodegradation, and thermal catalysis, are expensive and release toxic by-products [9,10]. The absorption method for VOCs exhibits insufficient storage capacity, requires frequent replacement, and produces easy desorption when heating [11,12]. Thermal catalysis and biodegradation also present some disadvantages, including a low catalyst efficiency, high operating temperatures, and high costs [13].

Photocatalysis represents a modern alternative to the traditional routes requiring low energy to operate, safer conditions, and is cost-effective. This method requires the use of photoactive materials and a corresponding light source to generate the super-oxidative species involved in the VOC decomposition [14–16]. Its main advantage is complete on-site pollutant mineralization without requiring additional storage equipment. The use of single-component photocatalysts such as TiO_2 [17,18], SnO_2 [19], CuO [20,21], and Ag_2O [22,23], induce limitations in terms of light absorbance spectrum or chemical stability. Studies have shown that heterostructures such as TiO_2/MnO_2 [24], Cu_xO/TiO_2 [25], TiO_2/SiO_2 [26,27], Ag_2O/TiO_2 [28], and ZnO/WO_3 [29] are able to efficiently separate the charge carriers in order to reduce recombination, increase charge mobility and use an extended light spectrum. However, the chemical stability and photocatalytic activity are drastically influenced by the working environment (pH, corrosive agents, etc.). Several papers indicate the use of g-C_3N_4 [30,31], g-C_4N_6 [32,33], and r-GO [34–36] in order to increase the specific active surface and, consequently, the photocatalytic efficiency.

This work presents the photocatalytic activity of titania-free material composed of $CuS/SnO_2/WO_3$ obtained by a three-step sol–gel method followed by spray deposition on the glass substrate. Acetaldehyde and formaldehyde were chosen as target VOC molecules due to their persistence in closed spaces and their negative impacts on human health. Both pollutants are considered to have carcinogenic potential with a direct impact on the kidneys and respiratory system. This work includes a comparative analysis between mono-component and multi-component samples in order to outline the synergic effect of semiconductor-based heterostructures. The correspondence between crystalline composition, morphology, and photocatalytic activity is also presented. The BET analysis indicates that the $CuS/SnO_2/WO_3$ heterostructure has a superior active surface compared with bare WO_3 and SnO_2/WO_3. The reusability tests show high photocatalytic efficiency for both pollutant molecules, which recommends this material as a sustainable alternative to the traditional methods.

2. Results and Discussion

2.1. Composition and Morphology

The X-ray diffraction analysis indicates the formation of stoichiometric compounds with a monoclinic structure for WO_3 (ICCD 83-0951), tetragonal structure for SnO_2 (cassiterite, ICCD 41-1445), and hexagonal structure for CuS (ICCD 03-1090), as presented in Figure 1. There are no indications regarding the formations of mixed oxides or non-stoichiometric forms of the heterostructure components. However, the presence of amorphous compounds, as well as element diffusion during the thermal treatment, cannot be excluded [37,38]. The insertion of metal oxides in the heterostructure precursors serves as the substrate for developing the following components. Based on previous reports [39,40], the metal oxide powder will facilitate the formation of the crystallization nucleus on the higher energy surface sites. It must be underlined that the CuS formation was stabilized in this form based on the step-by-step sulfur atmospheric treatment, which reduces the probability of oxygen insertion and allows an improved process control. The formation of CuS plays an important role in improving the Vis light absorption of the heterostructure assembly [41].

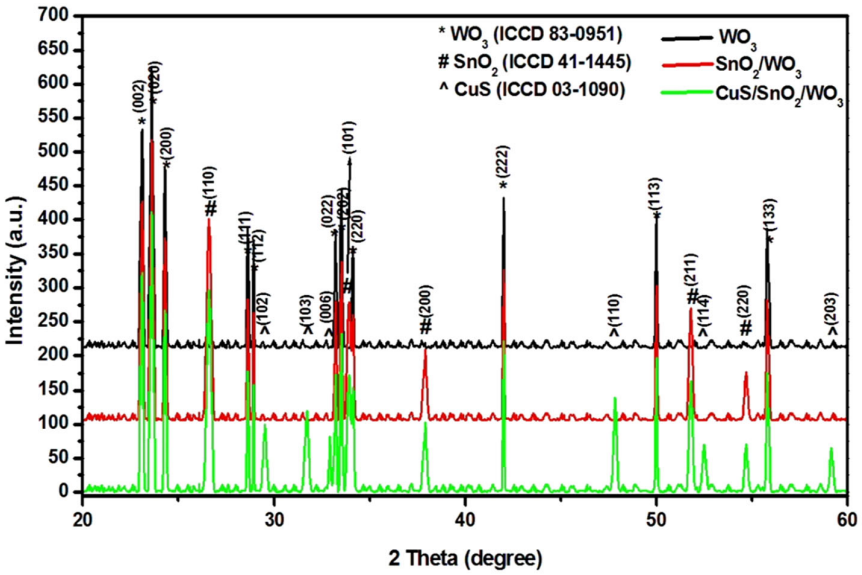

Figure 1. X-ray diffraction patterns of the samples.

The crystallite sizes were evaluated using the Scherrer formula, Equation (1), [42]:

$$D = \frac{0.9\lambda}{\beta \cos\theta}, \quad (1)$$

where β is the measured angular width at half maximum intensity (FWHM) of the peak, θ is the Braggs angle, and λ is the X-ray wavelength (1.5406 Å for $CuK_{\alpha 1}$). The evaluation was performed on the most significant plane relative to the line intensity for each component. Considering that the heterostructure semiconductors are used as the substrate, the crystallite size may influence the development of the following component. The results (see Table 1) indicate that similar crystal sizes for the metal oxide (WO_3 and SnO_2) compounds were subjected to relatively similar annealing temperatures (400 °C for WO_3 and 380 °C for SnO_2). The crystalline size of the metal oxides exhibits negligible changes after the inclusion in the following component precursor. Lower crystallite sizes were recorded for CuS, where the synthesis conditions are more restrictive in terms of the atmospheric conditions and temperature.

Table 1. Crystallite sizes of the photocatalysts components.

Samples	Crystallite Size (Å)		
	WO_3	SnO_2	CuS
WO_3	84.2	-	-
SnO_2/WO_3	83.7	78.1	-
$CuS/SnO_2/WO_3$	83.4	77.7	51.5

The SEM analyses indicate the formation of a fiber-like WO_3 morphology (Figure 2a) of around 1 μm diameter and variable length. As presented in Figure 2b, the SnO_2 will develop on the WO_3 fibers, which are completely covered at the end of the second synthesis step. The heterostructure morphology changes from fiber to granular (Figure 2c) after the CuS deposition, and the grains have various shapes and sizes. These changes are a consequence of the uniform surface coverage of the substrate obtained after each synthesis step. The porous morphology will be beneficial to the photocatalytic efficiency, allowing the formation of a larger liquid–solid interface, where the oxidation processes are developed [43–45]. The N_2 adsorption–desorption isotherm (Figure 3) indicates that the

CuS/SnO_2/WO_3 heterostructure exhibits a higher Brunauer–Emmett–Teller (BET) surface area (83.4 m^2/g and 0.023 cm^3/g pore volume) compared with WO_3 (34.1 m^2/g and 0.011 cm^3/g pore volume) and SnO_2/WO_3 (65.7 m^2/g and 0.016 cm^3/g pore volume).

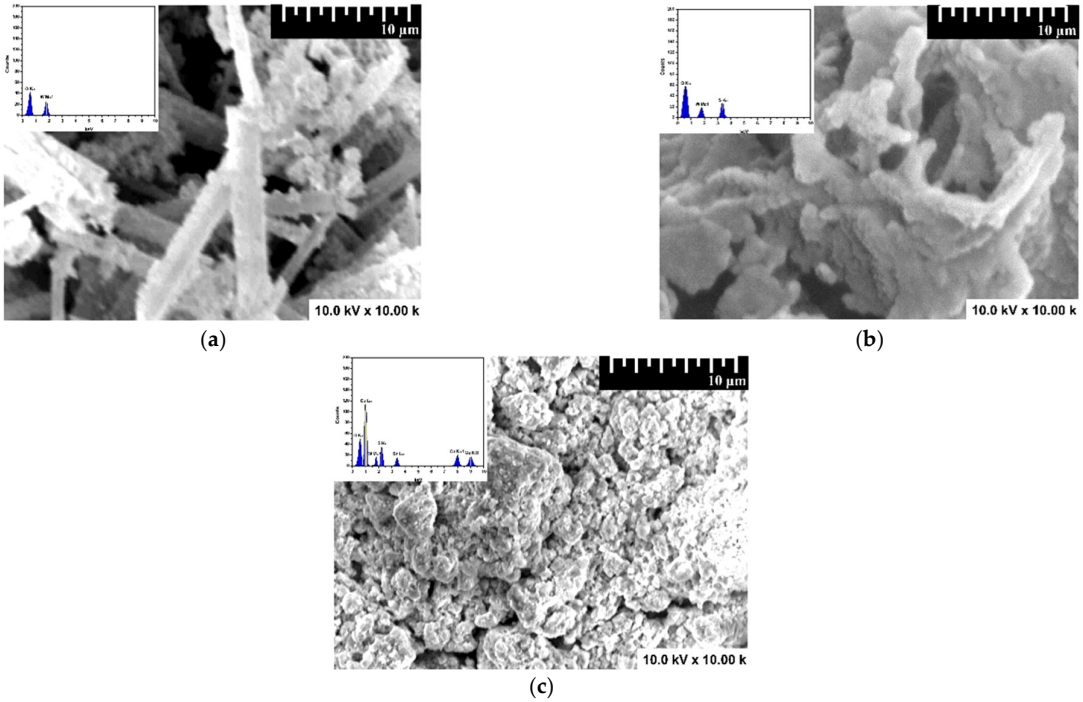

Figure 2. SEM pictures of the photocatalysts: (**a**) WO_3, (**b**) SnO_2/WO_3 and (**c**) CuS/SnO_2/WO_3 (inset EDX spectra).

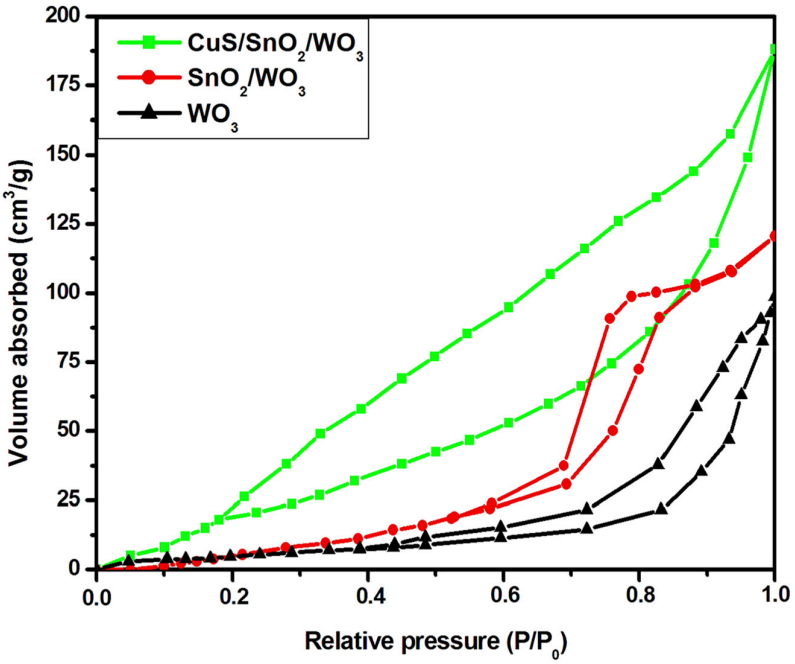

Figure 3. N2 adsorption–desorption isotherm.

The elemental composition of the samples was evaluated by EDX analysis (Table 2) in order to observe if the ratio of the components was preserved. The analysis was

conducted at different points, and the results indicate similar values, which confirm the homogeneity of the samples. Additionally, the results were compared with the theoretical values calculated based on the stoichiometry of each compound. The results indicate the presence of excess oxygen in both metal oxide components due to the long annealing periods at elevated temperatures [46,47]. After each deposition step, the W ratio decreases in relation to the other components (Sn and Cu). As expected, the CuS component exhibits a sulfur deficit due to the final thermal treatment conducted after the film deposition.

Table 2. Elemental composition of the photocatalysts.

Samples	Elemental Composition [% at.]						
	W	Sn	Cu	O	O_{th} [1]	S	S_{th} [1]
WO_3	24.6			75.4	73.8		
SnO_2/WO_3	11.2	16.4		72.4	66.2		
$CuS/SnO_2/WO_3$	9.7	11.8	13.5	54.8	52.7	10.2	13.5

[1] Stoichiometric theoretical content.

2.2. Indoor Air Photocatalytic Treatment

Acetaldehyde and formaldehyde were chosen as the reference VOCs based on their toxicity and resilience in households and indoor office air. These compounds are released into the air by different building materials, electronic devices, and cleaning products. Acetaldehyde and formaldehyde can cause eye irritation, respiratory diseases, and damage to the central nervous system [48–50]. Long-term exposures to acetaldehyde and formaldehyde may have carcinogenic effects, and the concentration of VOCs in indoor air should be drastically reduced [51,52]. The photocatalytic activity of all samples was evaluated under the same conditions of light radiation, catalyst dosage, irradiation period, and pollutant concentration.

2.2.1. VOCs degradation efficiency and kinetics

The photocatalytic evaluation (Figure 4) indicates that all samples are able to develop the oxidative species ($\cdot OH, \cdot O_2^-$) required for VOC degradation. However, the heterostructure mechanism can only use the charge carriers with enough potential to generate these oxidative species. The photogenerated electrons with a potential higher than −0.33 eV, as well as the photogenerated holes with a potential higher than +1.99 eV, are unable to promote the formation of oxidative species. The lowest photocatalytic efficiency (Figure 4a,b) corresponds to the WO_3 single-component sample, which was able to remove 49.8 ppm (31.5%) of acetaldehyde and 63.2 ppm (40.7%) of formaldehyde. Even if the light radiation contains both UV and Vis spectra, the WO_3 has a band gap of 3.3 eV, which limits the absorption range in the UV region. The synergic effect of coupled SnO_2/WO_3 semiconductors induces lower charge carrier recombination and increases the number of photogenerated charges [53,54]. The photocatalytic efficiency of the SnO_2/WO_3 sample is superior to that of the WO_3 single-component sample and attempts 41.1% for acetaldehyde (64.9 ppm) and 52.5% for formaldehyde (81.4 ppm). The highest photocatalytic activity corresponds to $CuS/SnO_2/WO_3$ heterostructure, where the CuS insertion with 1.8 eV band gap energy will extend the light absorption in the Vis region. The $CuS/SnO_2/WO_3$ heterostructure will benefit from a higher charge carrier concentration and mobility able to contribute to oxidative species development [55,56]. Consequently, the heterostructure photocatalytic efficiency was 69.2% for acetaldehyde and 78.5% for formaldehyde. The CO_2 evolution (Figure 4c,d) follows the same pattern as VOC removal, which indicates acetaldehyde and formaldehyde conversion by mineralization. Compared with other reported results (see Table 3), the photocatalytic efficiencies are competitive and could be considered for future applications. TiO_2-based photocatalysts may exhibit a higher efficiency function in these testing conditions and for this pollutant type. Small quantities of by-

products cannot be excluded as intermediary compounds formed during photocatalysis [56].

The mechanism of VOC photodegradation considers the following steps in Equations (2)–(5):

$$Heterostru\ cture + h\nu \rightarrow e^- + h^+, \quad (2)$$

$$h^+(Heterostructure) + H_2O \rightarrow HO\cdot + H^+, \quad (3)$$

$$O_2 + e^-(Heterostru\,cture) \rightarrow \cdot O_2^-, \quad (4)$$

$$CH_3CHO\ /\ H_2CO + HO\cdot + \cdot O_2^- \longrightarrow xCO_2 + yH_2O, \quad (5)$$

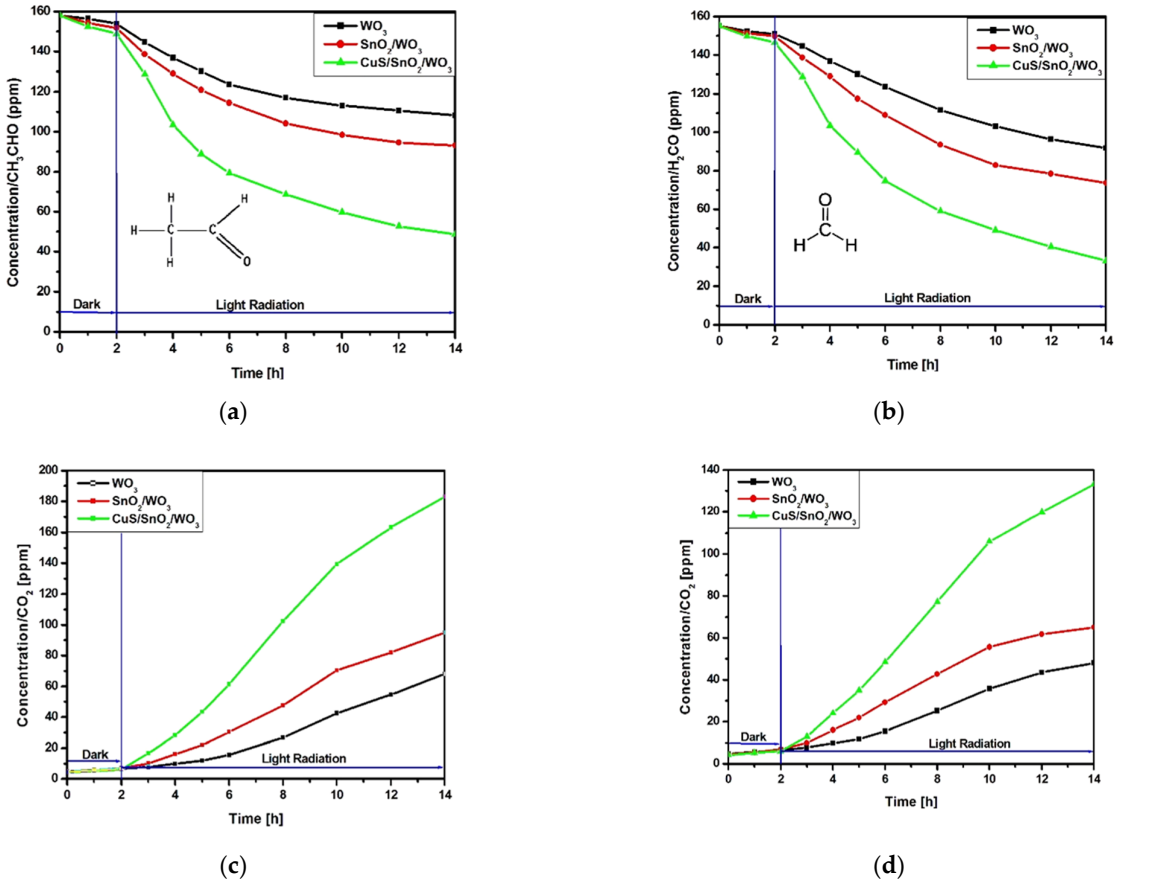

Figure 4. Photocatalytic removal of (**a**) acetaldehyde and (**b**) formaldehyde, and CO_2 evolution from (**c**) acetaldehyde and (**d**) formaldehyde degradation.

Table 3. Photocatalytic efficiency comparative results on VOC removal.

Materials	Pollutant Type and Concentration	Radiation Type and Intensity	Photocatalytic Efficiency and Degradation Time	Ref.
(rGO)-TiO_2	Acetaldehyde, 25 ppm o-xylene, 25 ppm	Vis, 200 W	42%, 160 min 54%, 160 min	[57]
Ag@TiO_2	Acetaldehyde, 500 ppm	UV, 260 W	72%, 4.8 min	[58]

Carbon quantum dots/TiO_2	Acetaldehyde, 500 ppm	Vis, 400 W	30%, 120 min	[59]
Rutile TiO_2	Acetaldehyde, 50 ppm	Vis, 260 W	65%, 65 min	[60]
Sn-$CaSn(OH)_6$(m)	Formaldehyde, 100 ppm	UV, 300 W	30%, 60 min	[61]
Doped TiO_2	Formaldehyde, 37%	LED, 25.7 W/m^2	43%, 120 min	[62]
Bi_2MoO_6-TiO/diatomite	Formaldehyde, 35 mg/m^3	Vis, 300 W	50%, 300 min	[63]
CuS/SnO_2/WO_3	Acetaldehyde, 170 ppm	UV–Vis, 300W	69,2%, 720 min	This
	Formaldehyde, 170 ppm		78,5%, 720 min	work

The kinetic evaluation was performed using the simplified Langmuir–Hinshelwood mathematical Equation (6), [64]:

$$\ln\frac{C}{C_0} = -kt \quad , \tag{6}$$

The results (Figure 5) show that the photocatalytic activity of CuS/SnO_2/WO_3 heterostructure was 3× faster than that of WO_3 and 2× faster than SnO_2/WO_3 for acetaldehyde removal. Similar results were observed for formaldehyde removal, where the CuS/SnO_2/WO_3 photocatalytic activity was 2.9× faster than that of the WO_3 single-component sample and 1.8× faster than that of the SnO_2/WO_3 sample. The small difference between the constant rates of the VOCs removal may be influenced by the chemical compatibility with the photocatalysts interface as well as oxidative species development during the irradiation. The R^2 factor is equal to or higher than 0.99, confirming that the model is representative regardless of the photocatalyst or pollutant molecule.

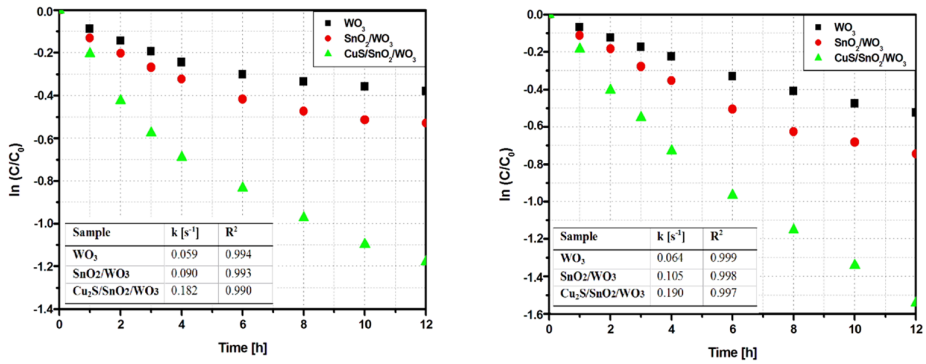

(**a**) (**b**)

Figure 5. Kinetics of (**a**) acetaldehyde and (**b**) formaldehyde photodegradation.

The reusability evaluation was undertaken in three cycle assessments (Figure 6) using the same testing conditions. The starting point of each cycle can present small variations due to the differences in reaching the absorption–desorption equilibrium. The results indicate a negligible variation of the photocatalytic activity (less than 2% abatement) for both acetaldehyde and formaldehyde removal. The stability of the photocatalytic activity indicates that the samples can be used in long-term photocatalytic applications without significant changes in the pollutant removal efficiency.

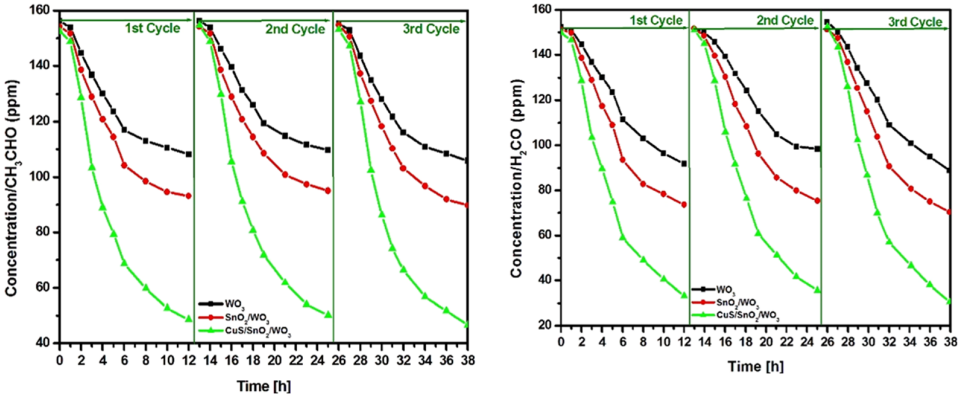

Figure 6. Reusability evaluation of the photocatalytic activity in three cycle assessments for (**a**) acetaldehyde and (**b**) formaldehyde removal.

2.2.2. Heterostructure Photocatalytic Mechanism

Understanding photogeneration and mobility mechanism of the charge carriers inside the CuS/SnO_2/WO_3 heterostructure will help to optimize and improve photocatalytic activity. The band energy diagram (Figure 7a) was obtained by considering the experimental values of the heterostructure band gap energy components (Figure 7b–d) and estimated based on the Wood and Tauc model. The band gap may submit a minor shift during the heterostructure development. The current methodology follows the description in the literature[65–67] and considers the band gap changes in the heterostructures internal energy field developed during the irradiation. The diagram includes the energy band position based on Equations (7)–(10), which consider several key parameters: E_e—represents the free electron energy vs. hydrogen; χ_{cation} (eV)—represents the absolute cationic electronegativity; χ_{cation} $(P.u.)$—represents the cationic specific electronegativity where *P.u.* corresponds to the Pauling units; E_g —represents the band gap energy; and $\chi_{semiconductor}$—represents the electronegativity of each semiconductor:

$$E_{VB} = \chi_{semiconductor} - E_e + 0.5E_g, \quad (7)$$

$$E_{CB} = E_{VB} - E_g, \quad (8)$$

$$\chi_{semiconductor}(eV) = 0.45 \times \chi_{cation}(eV) + 3.36 \quad (9)$$

$$\chi_{cation}(eV) = \frac{\chi_{cation}(P.u) + 0.206}{0.336} \quad (10)$$

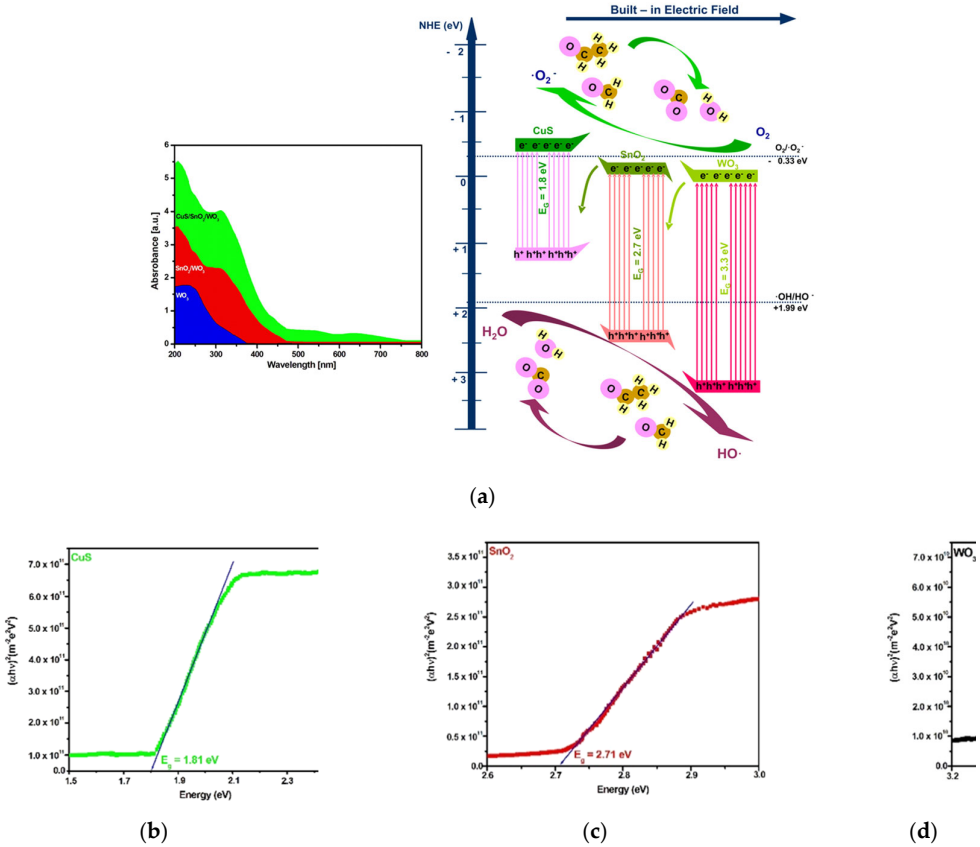

Figure 7. Heterostructure mechanism and absorption (**a**), and components band gap values (**b**–**d**).

The diagram can be described as a Z-scheme charge carrier transfer mechanism where the photogenerated electrons from the CuS conduction band (−0.41 eV) will temporarily migrate to the SnO_2 conduction band in order to be transferred to the WO_3 conduction band (+0.16 eV). Due to their potential, the electrons generated from the tin oxide and tungsten oxide conduction bands during irradiation cannot participate in the production of super-oxidative species ($\cdot O_2^-$). In the same way, the holes from the CuS valence band (+1.39 eV) generated during irradiation are not involved in the formation of oxidative species ($\cdot OH$). The major parts of these charges will recombine without influencing the photocatalytic process [68,69]. However, the electrons from the CuS conduction band, and the holes from the SnO_2 (+2.51 eV) and WO_3 (3.46 eV) valence bands generated during the light irradiation, have stronger redox abilities and are able to avoid recombination due to the electric field present in the charged separation area. The mobility of the charge carriers through the heterostructure is sustained by the interface of good semiconductors developed during their synthesis, causing a combined drift and diffusion effect.

3. Materials and Methods

3.1. Materials Synthesis and Heterostructure Deposition

3.1.1. Heterostructure Powder Synthesis

A three-step sol–gel method was used to develop the heterostructure, followed by thermal treatments corresponding to each component (Figure 8).

Step 1. WO_3 powder was synthesized using a precursor based on 0.9 mol hydrated tungsten hexachloride ($WCl_6.2H_2O$, 98.6%, AcrosOrganics, Gell, Germany) dissolved in a mixed solvent of 4.6 mol absolute methanol (CH_4O, 100%, Sigma Aldrich, Munich,

Germany) and 3.2 mol of 2-propanol (C_3H_8O, 100%, Sigma Aldrich, Munich, Germany). A yellow, homogenous solution was formed after 280 min of magnetic stirring. A slow addition of 0.31 mol sodium hydroxide (NaOH, 99.98%, Honeywell, Charlotte, NC, USA) was used to induce gel development. The relative pH of 11.5 was obtained during the NaOH addition, which works as a reducing agent and promotes condensation to form the gel. Adding too much NaOH stabilized the anions, and the formed gel may be redissolved. The gel was then preserved in the dark for 16 h, and the yellow precipitate (Figure 8—Step 1) was centrifuged. The final powder was thermally treated at 400 °C for 3.5 h.

Step 2. SnO_2/WO_3 powder was obtained by dispersing the previously obtained WO_3 powder into a precursor composed of 0.9 mol tin tetrachloride ($SnCl_4$, 99.8%, Sigma Aldrich, Munich, Germany) dissolved in 3.8 mol of 2-propanol (C_3H_8O, 100%, Sigma Aldrich, Munich, Germany). The mixture was covered and magnetically stirred for 240 min to ensure the WO_3 particles were uniformly dispersed into the SnO_2 precursor. Then, 0.20 mol of sodium hydroxide (NaOH, 99.98%, Honeywell, Charlotte, NC, USA) was added drop by drop until a yellowish-white precipitate was obtained. The relative pH of the sol–gel was 11.3, where NaOH works as a reducing agent. The precipitate (Figure 8—Step 2) was centrifuged and annealed at 380 °C for 6 h.

Step 3. $CuS/SnO_2/WO_3$ heterostructure was developed by inserting the previously obtained SnO_2/WO_3 powder into a solution containing 0.27 mol of copper nitrate (99.7%, $Cu(NO_3)_2$, Scharlau, Barcelona, Spain), 0.6 mol of sodium thiosulfate (99.8%, $Na_2S_2O_3$, Scharlau, Barcelona, Spain) and deionized water. After 50 min of magnetic stirring, the obtained gel was preserved in a dark room for 5.5 h until complete precipitation was achieved. After centrifugation, the brown powder still contained intermediary products (CuS_2O_3 and $Cu_2S_2O_3$) and was heated at 130 °C in a ceramic-based capsule containing a sulfur (sulfur, 99%, Sigma Aldrich, Munich, Germany) atmosphere. The dark powder (Figure 8—Step 3) was cooled at a rate of 5 °C/h until it reached room temperature.

3.1.2. Film Deposition

The heterostructure films (Figure 8—Step 4) were developed using the cold spray deposition technique. The spray precursor was obtained by dispersing 40 mg of powder (WO_3, SnO_2/WO_3, and $CuS/SnO_2/WO_3$) in a 40 mL mixture of absolute ethanol by an ultrasound bath. Triton X was added (0.1 mL) into the precursor, and the mixture was stirred for 60 min. The microscope glass substrate (2 × 2 cm^2 pieces) was firstly degreased with surfactants. Then, the substrates were cleaned by successive immersion in ethanol and acetone. The clean substrates were pre-heated at 40 °C for 100 min, and then the precursor was sprayed at 0.35 bars. Breaks of 15 min were observed between each deposition sequence in order to allow solvent evaporation. For each microscope glass substrate, 0.02 g of powder was used to obtain the coating.

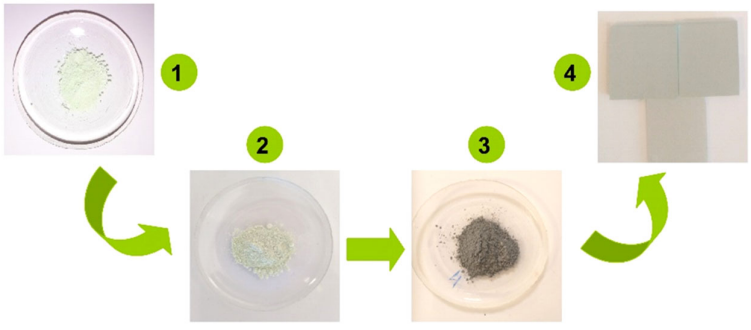

Figure 8. Powder and film samples.

3.2. Photocatatalytic Experiments

The photocatalytic experiments were conducted in a cylindrical quart air-proof reactor. The UV–Vis light irradiance was provided at 300 W Xenon lamp intensity. The distance between the lamp and the sample was 5 cm, and the irradiance on the sample surface was 28 mW/cm^2. A heterostructure sample of 2 × 2 cm^2 was inserted into the reactor, and dry air was used to purge the reactor chamber at a continuous flow rate for 35 min. When the reactor was closed, the acetaldehyde or formaldehyde was injected (170 ppm), and the system was kept in the dark for 2 h to reach the absorption–desorption equilibrium. Then, the samples were continuously exposed to light irradiation for 12 h, and the gas concentration was evaluated hourly using gas chromatography.

3.3. Materials Characterization

The presence of crystalline structures was evaluated with an X-ray diffractometer (Rigaku, Miniflex X-Ray diffractometer, Tokyo, Japan) using a 40 kV CuKα source (I = 1.54 Å, 100 mA). The morphology of the samples was investigated at an accelerated voltage of 10 kV in a high-vacuum regime using scanning electron microscopy (SEM, S-3400 N-type 121 II Hitachi model, Tokyo, Japan). Field-emission scanning electron microscopy (FESEM, SU8010, Fukuoka, Japan) was also involved in the morphological investigations. The active surface area and pore size were evaluated by N_2 adsorption–desorption isotherm analysis (Tristar II Plus, Micromeritics, Georgia, GA, USA) with a porosimeter. The heterostructure components band gap was investigated using UV–Vis spectrometry (Lambda 950, Perkin Elmer, Waltham, MA, USA). The VOCs (acetaldehyde and formaldehyde) and CO2 concentrations were measured by gas chromatography (GC-2014, Shimadzu, Maryland, CO, USA).

4. Conclusions

A Z-scheme heterostructure based on CuS/SnO_2/WO_3 was developed in three sol–gel steps, using the metal oxides as nucleation sites for the following components. The final powder was used to prepare the precursor required for film deposition by spray deposition. The metal oxide samples exhibit crystalline structures and relatively similar crystallite sizes without any evidence of non-stoichiometric compounds. The WO_3 single-component sample morphology consists of fibers that serve as the substrate for SnO_2 development. The CuS/SnO_2/WO_3 heterostructure possesses the highest active surface (83.4 m^2/g) and is characterized by a dense morphology with grains of various shapes and sizes.

The photocatalytic activity evaluation indicates that the WO3 single-component sample is able to remove 41.1% of acetaldehyde (64.9 ppm) and 52.5% of formaldehyde (81.4 ppm). However, the CuS/SnO_2/WO_3 heterostructure exhibits a superior photocatalytic activity compared with other reported values, due to larger light spectrum absorption and a lower charge carrier recombination rate, enabling the removal of 69.2% of acetaldehyde and 78.5% of formaldehyde. The reusability evaluation shows a negligible variation of the photocatalytic activity after three cycle assessments for both acetaldehyde and formaldehyde removal. During light irradiation, the heterostructure benefits from the redox ability of the CuS conduction band electron and the SnO_2/WO_3 valence band holes, which can generate the oxidative species required for the removal of VOCs. Optimizing the heterostructure photocatalytic efficiency toward the VOCs is necessary and requires intrinsic changes to improve the photogeneration and mobility of charge carriers .

Author Contributions: Conceptualization, A.E.; Methodology, A.E.; Software, V.S.; Investigation, A.E.; Resources, A.E.; Data curation, A.E.; Writing—original draft preparation, A.E.; Writing—review and editing, A.E.; Visualization, V.S.; Supervision, A.E.; Project administration, A.E.; Funding acquisition, A.E. All authors have read and agreed to the published version of the manuscript.

Funding: This work was supported by a grant from the Ministry of Research, Innovation and Digitization, CNCS-UEFISCDI, project number PN-III-P4-PCE-2021-1020 (PCE87) within PNCDI III.

Data Availability Statement: Data presented in this study are available upon request from the corresponding author.

Acknowledgments: The authors acknowledge the support given by the Tokyo University of Science for our experimental investigations.

Conflicts of Interest: The authors declare no conflict of interest.

References

1. Lu, C.; Deng, M.; Deng, Q. Effect of outdoor air pollution and indoor environmental factors on small for gestational age. *Build. Environ.* **2021**, *206*, 108399.
2. Edginton, S.; O'Sullivan, D.E.; Lougheed, M.D. The effect of acute outdoor air pollution on peak expiratory flow in individuals with asthma: A systematic review and meta-analysis. *Environ. Res.* **2021**, *192*, 110296.
3. Havet, A.; Hulo, S.; Dauchet, L. Residential exposure to outdoor air pollution and adult lung function, with focus on small airway obstruction. *Environ. Res.* **2020**, *183*, 109161.
4. Ye, M.; Chen, L.; Liu, X.; Xu, W.; Zhu, T.; Chen, G. Catalytic Oxidation of Chlorobenzene over Ruthenium-Ceria Bimetallic Catalysts. *Catalysts* **2018**, *8*, 116.
5. Li, X.; Sun, L.; Sui, H.; He, L.; Yuan, W.; Han, Z. A Novel Polymeric Adsorbent Embedded with Phase Change Materials (PCMs) Microcapsules: Synthesis and Application. *Nanomaterials* **2019**, *9*, 736.
6. Chang, S.J.; Wi, S.; Jeong, S.-G.; Kim, S. Evaluation of the Adsorption Performance and Sustainability of Exfoliated Graphite Nanoplatelets (xGnP) for VOCs. *Materials* **2015**, *8*, 7615–7621.
7. Enesca, A.; Andronic, L.; Duta, A. Optimization of Opto-Electrical and Photocatalytic Properties of SnO2 Thin Films Using Zn2+ and W6+ Dopant Ions. *Catal. Lett.* **2012**, *142*, 224–230.
8. Jia, L.; Shi, J.; Xing, B. VOCs adsorption on activated carbon with initial water vapor contents: Adsorption mechanism and modified characteristic curves. *Sci. Total Environ.* **2020**, *731*, 139184.
9. Liang, Q.; Bao, X.; Chu, Y. Imaging VOC distribution in cities and tracing VOC emission sources with a novel mobile proton transfer reaction mass spectrometer. *Environ. Pollut.* **2020**, *265*, 114628.
10. Arı, A.; Arı, P.E.; Gaga, E.O. Source characterization and risk assessment of occupational exposure to volatile organic compounds (VOCs) in a barbecue restaurant. *Build. Environ.* **2020**, *174*, 106791.
11. Wantz, E.; Kane, A.; Couvert, A. A mathematical model for VOCs removal in a treatment process coupling absorption and biodegradation. *Chem. Eng. J.* **2021**, *423*, 130106.
12. Sansotera, M.; Kheyli, S.G.M.; Navarrini, W. Absorption and photocatalytic degradation of VOCs by perfluorinated ionomeric coating with TiO2 nanopowders for air purification. *Chem. Eng. J.* **2019**, *361*, 885–896.
13. Wei, L.; Yu, C.; Ji, H. Recent advances in VOCs and CO removal via photothermal synergistic catalysis. *Chin. J. Catal.* **2021**, *42*, 1078–1095.
14. Wang, Z.; Xie, X.; Sun, J. Difference of photodegradation characteristics between single and mixed VOC pollutants under simulated sunlight irradiation. *J. Photochem. Photobiol. A* **2019**, *384*, 112029.
15. Truc, N.T.T.; Pham, T.D.; Trang, H.T. Superior activity of Cu-NiWO4/g-C3N4 Z direct system for photocatalytic decomposition of VOCs in aerosol under visible light. *J. Alloys Compd.* **2019**, *798*, 12–18.
16. Vikrant, K.; Park, C.M.; Jeon, E.C. Recent advancements in photocatalyst-based platforms for the destruction of gaseous benzene: Performance evaluation of different modes of photocatalytic operations and against adsorption techniques. *J. Photochem. Photobiol. C* **2019**, *41*, 100316.
17. Heydari, G.; Hollman, J.; Achari, G.; Langford, C.H. Comparative Study of Four TiO2-Based Photocatalysts to Degrade 2,4-D in a Semi-Passive System. *Water* **2019**, *11*, 621.
18. Ehlert, M.; Radtke, A.; Topolski, A.; Śmigiel, J.; Piszczek, P. The Photocatalytic Activity of Titania Coatings Produced by Electrochemical and Chemical Oxidation of Ti6Al4V Substrate, Estimated According to ISO 10678:2010. *Materials* **2020**, *13*, 2649.
19. Dudita, M.; Bogatu, C.; Enesca, A.; Duta, A. The influence of the additives composition and concentration on the properties of SnOx thin films used in photocatalysis. *Mater. Lett.* **2011**, *65*, 2185–2189.
20. Lu, H.; Zhang, L.; Ma, J.; Alam, N.; Zhou, X.; Ni, Y. Nano-Cellulose/MOF Derived Carbon Doped CuO/Fe_3O_4 Nanocomposite as High Efficient Catalyst for Organic Pollutant Remedy. *Nanomaterials* **2019**, *9*, 277.
21. Pu, S.; Wang, H.; Zhu, J.; Li, L.; Long, D.; Jian, Y.; Zeng, Y. Heterostructure Cu2O/(001)TiO2 Effected on Photocatalytic Degradation of Ammonia of Livestock Houses. *Catalysts* **2019**, *9*, 267.
22. Pang, C.; Mackevica, A.; Tian, J.; Feng, H.; Li, Z.; Baun, A. Release of Ag/ZnO Nanomaterials and Associated Risks of a Novel Water Sterilization Technology. *Water* **2019**, *11*, 2276.
23. Kumar, R.; El-Shishtawy, R.M.; Barakat, M.A. Synthesis and Characterization of Ag-Ag_2O/TiO_2@polypyrrole Heterojunction for Enhanced Photocatalytic Degradation of Methylene Blue. *Catalysts* **2016**, *6*, 76.
24. Chen, H.; Liu, X.Y.; Zhang, Y.X. Facile biphasic synthesis of TiO_2–MnO_2 nanocomposites for photocatalysis. *Ceram. Int.* **2016**, *42*, 19425–19428.
25. Kong, L.; Zhang, X.; Li, L. Synergic effects of CuxO electron transfer co-catalyst and valence band edge control over TiO2 for efficient visible-light photocatalysis. *Chin. J. Catal.* **2017**, *38*, 2120–2131.

26. Huang, F.; Hao, H.; Lang, X. Dye-TiO2/SiO2 assembly photocatalysis for blue light-initiated selective aerobic oxidation of organic sulfides. *Chem. Eng. J.* **2021**, *423*, 129419.
27. Theil, F.; Dellith, A.; Dietzek, B. Ru dye functionalized Au–SiO_2@TiO_2 and Au/Pt–SiO_2@TiO_2 nanoassemblies for surface-plasmon-induced visible light photocatalysis. *J. Colloid Interface Sci.* **2014**, *421*, 114–121.
28. Xu, W.; Tang, H.; Shen, Y. Enhanced photocatalytic activity of TiO_2/Ag_2O heterostructures by optimizing the separation of electric charges. *Vacuum* **2021**, *190*, 110283.
29. Li, D.; Haneda, H. Photocatalysis of sprayed nitrogen-containing Fe_2O_3–ZnO and WO_3–ZnO composite powders in gas-phase acetaldehyde decomposition. *J. Photochem. Photobiol. A Chem.* **2003**, *160*, 203–212.
30. Zhao, W.; Yang, X.; Liu, C.; Qian, X.; Wen, Y.; Yang, Q.; Sun, T.; Chang, W.; Liu, X.; Chen, Z. Facile Construction of All-Solid-State Z-Scheme g-C3N4/TiO2 Thin Film for the Efficient Visible-Light Degradation of Organic Pollutant. *Nanomaterials* **2020**, *10*, 600.
31. Li, Z.; Meng, X.; Zhang, Z. An Effective Approach to Improve the Photocatalytic Activity of Graphitic Carbon Nitride via Hydroxyl Surface Modification. *Catalysts* **2019**, *9*, 17.
32. Jiao, Z.; Wang, Y.; Huang, W. Effect of the activator on the performance of alkali-activated slag mortars with pottery sand as fine aggregate. *Constr. Build. Mater.* **2019**, *197*, 83–90.
33. Zhang, Y.; Xu, C.; Lu, X. Experimental study of hysteretic behaviour for concrete-filled square thin-walled steel tubular columns. *J. Constr. Steel Res.* **2007**, *63*, 317–325.
34. Imran, M.; Alam, M.M.; Irshad, K. Highly photocatalytic active r-GO/Fe_3O_4 nanocomposites development for enhanced photocatalysis application: A facile low-cost preparation and characterization. *Ceram. Int.* **2021**, *47*, 31973–31982.
35. Noor, S.; Sajjad, S.; Long, M. Energy harvesting for electrochemical OER and solar photocatalysis via dual functional GO/TiO_2-NiO nanocomposite. *J. Clean. Prod.* **2020**, *277*, 123280.
36. Chen, Y.H.; Wang, B.K.; Hou, W.C. Graphitic carbon nitride embedded with graphene materials towards photocatalysis of bisphenol A: The role of graphene and mediation of superoxide and singlet oxygen. *Chemosphere* **2021**, *278*, 130334.
37. Enesca, A.; Duta, A. Tailoring WO3 thin layers using spray pyrolysis technique. *Phys. Status Solidi C* **2008**, *5*, 3499–3502.
38. Zhang, Y.; Wang, D.; Zheng, W. One-step synthesized CuS and MWCNTs composite as a highly efficient counter electrode for quantum dot sensitized solar cells. *Mater. Des.* **2018**, *160*, 870–875.
39. Yu, J.; Lee, T.I.; Misra, M. Synergetic impact of surface plasmon hot electron and CuS nanolayer of CuS/Au/ZnO core-shell nanorods for the degradation of toxic pollutant. *J. Ind. Eng. Chem.* **2018**, *66*, 468–477.
40. Peng, J.; Lu, X.; Yao, G. Degradation of atrazine by persulfate activation with copper sulfide (CuS): Kinetics study, degradation pathways and mechanism. *Chem. Eng. J.* **2018**, *354*, 740–752.
41. Kovacı, H.; Akaltun, Y.; Çelik, A. Investigation of the usage possibility of CuO and CuS thin films produced by successive ionic layer adsorption and reaction (SILAR) as solid lubricant. *Surf. Coat. Technol.* **2018**, *344*, 522–527.
42. Jilani, A.; Ansari, M.O.; Rehman, G.; Shakoor, M.B.; Hussain, S.Z.; Othman, M.H.D.; Ahmad, S.R.; Dustgeer, M.R.; Alshahri, A. Phenol removal and hydrogen production from water: Silver nanoparticles decorated on polyaniline wrapped zinc oxide nanorods. *J. Ind. Eng. Chem.* **2022**, *109*, 347–358.
43. Wu, Q.; Liu, X.; Yang, Z. Biotemplate synthesis and photocatalysis performance of multilayer porous $ZnWO_4$ nano-photocatalyst with rose petals as template. *Colloids Surf. A Physicochem. Eng. Asp.* **2021**, *629*, 127459.
44. Wang, Y.; Chen, B.B.; Li, D.W. Carbon dots induced in-situ formation of porous europium micro-networks with enhanced photocatalysis. *J. Colloid Interface Sci.* **2022**, *606*, 600–606.
45. Mouchaal, Y.; Enesca, A.; Mihoreanu, C.; Khelil, A.; Duta, A. Tuning the opto-electrical properties of SnO_2 thin films by Ag+1 and In+3 co-doping. *Mater. Sci. Eng. B* **2015**, *199*, 22–29.
46. Wang, P.; Li, X.; Liu, S. Piezotronic effect and oxygen vacancies boosted photocatalysis C–N coupling of benzylamine. *Nano Energy* **2021**, *83*, 105831.
47. Feng, C.; Tang, L.; Wang, J. Maintaining stable LSPR performance of $W_{18}O_{49}$ by protecting its oxygen vacancy: A novel strategy for achieving durable sunlight driven photocatalysis. *Appl. Catal. B Environ.* **2020**, *276*, 119167.
48. Lachenmeier, D.W.; Salaspuro, M. ALDH2-deficiency as genetic epidemiologic and biochemical model for the carcinogenicity of acetaldehyde. *Regul. Toxicol. Pharm.* **2017**, *86*, 128–136.
49. Kanjanasiranont, N.; Prueksasit, T.; Morknoy, D. Inhalation exposure and health risk levels to BTEX and carbonyl compounds of traffic policeman working in the inner city of Bangkok, Thailand. *Atmos. Environ.* **2017**, *152*, 111–120.
50. Gong, Y.; Wei, Y.; Xu, B. Health risk assessment and personal exposure to Volatile Organic Compounds (VOCs) in metro carriages—A case study in Shanghai, China. *Sci. Total Environ.* **2017**, *574*, 1432–1438.
51. Bari, M.A.; Kindzierski, W.B. Ambient volatile organic compounds (VOCs) in communities of the Athabasca oil sands region: Sources and screening health risk assessment. *Environ. Pollut.* **2018**, *235*, 602–614.
52. Dai, W.; Zhong, H.; Ho, K.F. Characterization and health risk assessment of airborne pollutants in commercial restaurants in northwestern China: Under a low ventilation condition in wintertime. *Sci. Total Environ.* **2018**, *633*, 308–316.
53. Enesca, A.; Isac, L.; Duta, A. Charge carriers injection in tandem semiconductors for dyes mineralization. *App. Catal. B* **2015**, *162*, 352–363.
54. Wang, H.; Cui, W.; Dong, F. Interfacial activation of reactants and intermediates on $CaSO_4$ insulator-based heterostructure for efficient photocatalytic NO removal. *Chem. Eng. J.* **2020**, *390*, 124609.

55. Ji, H.; Du, P.; Liu, W. 2D/1D graphitic carbon nitride/titanate nanotubes heterostructure for efficient photocatalysis of sulfamethazine under solar light: Catalytic "hot spots" at the rutile–anatase–titanate interfaces. *Appl. Catal. B Environ.* **2020**, *263*, 118357.
56. Su, J.; Yu, S.; Zhao, W. Enhanced visible light photocatalytic performances of few-layer MoS_2@TiO_2 hollow spheres heterostructures. *Mater. Res. Bull.* **2020**, *130*, 110936.
57. Lin, W.; Xie, X.; Wang, X.; Wang, Y.; Segets, D.; Sun, J. Efficient adsorption and sustainable degradation of gaseous acetaldehyde and o-xylene using rGO-TiO2 photocatalyst. *Chem. Eng. J.* **2018**, *349*, 708–718.
58. Zeng, Q.; Xie, X.; Wang, X.; Wang, Y.; Lu, G.; Pui, D.Y.H.; Sun, J. Enhanced photocatalytic performance of Ag@TiO_2 for the gaseous acetaldehyde photodegradation under fluorescent lamp. *Chem. Eng. J.* **2018**, *341*, 83–92.
59. Hu, Y.; Xie, X.; Wang, X.; Wang, Y.; Zeng, Y.; Pui, D.Y.H.; Sun, J. Visible-Light Upconversion Carbon Quantum Dots Decorated TiO2 for the Photodegradation of Flowing Gaseous Acetaldehyde. *Appl. Surf. Sci.* **2018**, *440*, 266–274.
60. Zeng, Q.; Wang, X.; Xie, X.; Mahmood, A.; Lu, G.; Wang, Y.; Sun, J. Band bending of TiO2 induced by O-xylene and acetaldehyde adsorption and its effect on the generation of active radicals. *J. Colloid Interface Sci.* **2020**, *572*, 374–383.
61. Wang, H.; Dong, X.; Tang, R.; Li, J.; Sun, Y.; Wanga, Z.; Kimb, K.H.; Dong, F. Selective breakage of CH bonds in the key oxidation intermediates of gaseous formaldehyde on self-doped $CaSn(OH)_6$ cubes for safe and efficient photocatalysis. *Appl. Catal. B* **2020**, *277*, 119214.
62. Laciste, M.T.; Luna, M.D.G.; Tolosa, N.C.; Lu, M.C. Degradation of gaseous formaldehyde via visible light photocatalysis using multi-element doped titania nanoparticles. *Chemosphere* **2017**, *182*, 174–182.
63. Yuan, F.; Yang, R.; Li, C.; Zhang, X.; Sun, Z. Enhanced visible-light properties of TiO_2/diatomite composite over varied bismuth semiconductors modification for formaldehyde photodegradation: A comparative study. *Sep. Purif. Technol.* **2022**, *297*, 121477.
64. Jilani, A.; Hussain, S.Z.; Melaibari, A.A.; Abu-Hamdeh, N.H. Development and Mechanistic Studies of Ternary Nanocomposites for Hydrogen Production from Water Splitting to Yield Sustainable/Green Energy and Environmental Remediation. *Polymers* **2022**, *14*, 1290.
65. Baneto, M.; Enesca, A.; Mihoreanu, C.; Lare, Y.; Jondo, K.; Napo, K.; Duta, A. Effects of the growth temperature on the properties of spray deposited $CuInS_2$ thin films for photovoltaic applications. *Ceram. Int.* **2015**, *41*, 4742–4749.
66. Gao, C.; Li, J.; Shan, Z.; Huang, F.; Shen, H. Preparation and visible-light photocatalytic activity of In_2S_3/TiO_2 composite. *Mater. Chem. Phys.* **2010**, *122*, 183–187.
67. Mise, T.; Nakada, T. Low temperature growth and properties of Cu–In–Te based 433 thin films for narrow bandgap solar cells. *Thin Solid Films* **2010**, *518*, 5604–5609.
68. Wu, J.; Wang, W.; Xue, H. Piezotronic effect boosted photocatalytic performance of heterostructured $BaTiO_3$/TiO_2 nanofibers for degradation of organic pollutants. *Nano Energy* **2020**, *77*, 105122.
69. Wang, X.; Wang, Y.; Tang, W. Designing strained C_2N/GaTe(InTe) heterostructures for photovoltaic and photocatalytic application. *J. Alloy. Compd.* **2020**, *816*, 152559.